SIAM J. SCI. COMPUT.
Vol. 40, No. 2, pp. A903–A928

NEW FINITE VOLUME WEIGHTED ESSENTIALLY NONOSCILLATORY SCHEMES ON TRIANGULAR MESHES*

JUN ZHU† AND JIANXIAN QIU‡

Abstract. In this paper, we design a new type of high order finite volume weighted essentially nonoscillatory (WENO) schemes to solve hyperbolic conservation laws on triangular meshes. The main advantages of these schemes are their compactness and robustness and that they could maintain a good convergence property for some steady state problems. Compared with the classical finite volume WENO schemes [C. Hu and C.-W. Shu, *J. Comput. Phys.*, 150 (1999), pp. 97–127], the optimal linear weights are independent of the topological structure of the triangular meshes and can be any positive numbers with the one requirement that their summation is one. This is the first time any high order accuracy with the usage of only five unequal sized stencils in a spatial reconstruction methodology on triangular meshes has been obtained. Extensive numerical results are provided to illustrate the good performance of such new finite volume WENO schemes.

Key words. weighted essentially nonoscillatory scheme, triangular mesh, finite volume scheme, high order accuracy, steady state problem

AMS subject classifications. 65M60, 35L65

DOI. 10.1137/17M1112790

1. Introduction.

In this paper, we study the high order finite volume numerical methods for solving the nonlinear hyperbolic conservation laws,

$$\begin{cases} u_t + f(u)_x + g(u)_y = 0, \\ u(x, y, 0) = u_0(x, y), \end{cases} \tag{1.1}$$

on triangular meshes. Essentially nonoscillatory (ENO) and weighted ENO (WENO) schemes are high order numerical methods for solving (1.1). ENO schemes were designed by Harten et al. [11, 23, 24]. The first WENO scheme was constructed by Liu, Osher, and Chan [16] for a third order finite volume version. In 1996, the third and fifth order finite difference WENO schemes were constructed by Jiang and Shu [13] in multispace dimensions, with a general framework for the design of smoothness indicators and nonlinear weights. Some classical finite volume WENO schemes on structured and unstructured meshes were developed in [8, 12, 14, 18, 20]. Among them, a key point in WENO schemes is a linear combination of lower order fluxes or reconstructions to obtain a higher order approximation. Both ENO and WENO schemes use the idea of adaptive stencils to automatically achieve high order accuracy and a nonoscillatory property near strong discontinuities. For the system case, such as Euler equations, WENO schemes use the methodologies of the local characteristic decompositions and flux splitting to avoid spurious oscillations near the

*Submitted to the journal's Methods and Algorithms for Scientific Computing section January 23, 2017; accepted for publication (in revised form) January 17, 2018; published electronically March 27, 2018.

http://www.siam.org/journals/sisc/40-2/M111279.html

Funding: This first author's work was partly supported by NSFC grant 11372005. The second author's work was partly supported by NSAF grant U1630247 and NSFC grant 11571290.

†College of Science, Nanjing University of Aeronautics and Astronautics, Nanjing, Jiangsu 210016, People's Republic of China (zhujun@nuaa.edu.cn).

‡Corresponding Author. School of Mathematical Sciences and Fujian Provincial Key Laboratory of Mathematical Modeling and High-Performance Scientific Computing, Xiamen University, Xiamen, Fujian 361005, People's Republic of China (jxqiu@xmu.edu.cn).

shocks or contact discontinuities. Harten [9] first presented two-dimensional finite volume ENO schemes. Then Casper [3] and Casper and Atkins [4] studied the finite volume approach in developing multidimensional high order accurate ENO schemes for hyperbolic conservation laws. The most important and main frameworks of two-dimensional finite volume WENO schemes on triangular meshes were proposed by Hu and Shu [12]. In their paper, they proposed a third order WENO scheme by using a combination of nine linear polynomials and a fourth order WENO scheme by using a combination of six quadratic polynomials, giving a new way of measuring two-dimensional smoothness of numerical solutions which was different from the expressions specified in [1, 8]. But the skills of maintaining positive linear weights for the third order and fourth order finite volume WENO schemes were too sophisticated to be fulfilled and such circumstance resulted in the lack of engineering applications as pointed out in [12]. Qiu and Shu [19] gave a framework of two-dimensional finite volume WENO schemes on structured meshes, in which they expressed the construction principle of the linear weights in detail and the free parameters were determined in a least squares sense. By doing so, the linear weights were unique and positive. After the analysis of the finite volume WENO schemes in the literature, generally speaking, there are two different kinds of finite volume WENO schemes: one type includes the WENO schemes [6, 7, 8, 25] whose order of accuracy is not higher than that of the reconstruction on each smaller spatial stencils. Their linear weights are artificially set as any positive numbers on the condition that the summation is one for sustaining the conservative property without needing to maintain the order accuracy, except for keeping nonlinear stability and avoiding spurious oscillations robustly. As stated in [6], Dumbser and Käser proposed the WENO schemes which did not suffer from the problem of negative linear weights, since the linear weights were not used to increase accuracy. They could get arbitrary high order schemes using derivatives on triangular or tetrahedral cells with large-scale spatial stencils. The second type includes the WENO schemes [12, 20, 28] whose order of accuracy is higher than that of the reconstruction on each smaller stencils. This type of WENO scheme that is more difficult to construct mainly originates in solving linear systems for getting linear weights; however, they could have a more compact spatial stencil than previous type of WENO schemes to achieve the same order accuracy in a smooth region.

Based on these evaluations, new third order and fourth order finite volume WENO schemes which have all the advantages and avoid the drawbacks of two different types of WENO schemes are presented in this paper. Comparing with [6], we can use a more compact spatial stencil to achieve the same order of accuracy in a smooth region. And we can set the linear weights as any positive numbers requiring their summation is one, in comparison with [12, 20, 28], where the linear weights for all reconstruction points must be computed by solving a linear system without conserving the positive property, and only the mostly near-uniform meshes can guarantee the linear weights are positive as stated in [12]. The basic flowchart of the third order finite volume WENO scheme is briefly narrated as follows. When constructing such a scheme, we use a big central spatial stencil which contains at least six triangular cells including the target cell to reconstruct a quadratic polynomial based on the conservative variables defined on triangular cells and use four four-cell small stencils including the target cell to reconstruct four linear polynomials in a least squares sense. Then the quadratic polynomial is modified by the subtraction of four linear polynomials with suitable parameters, so as to keep the third order approximations at any points inside the target cell in a smooth region [12, 22, 30, 31]. Hereafter, any positive linear weights are

chosen on the condition that their summation is one. And we should keep a relative equilibrium between the sharp shock transitions and spurious oscillations in the nonsmooth region. After computing the smoothness indicators and nonlinear weights, together with the third order TVD Runge–Kutta time discretization method [23], such a new WENO scheme is designed in both space and time. As analyzed in [17], Liu and Zhang found that it was hard to design a robust WENO scheme when facing distorted local mesh geometries or degenerate cases when the mesh quality varied for complex domain geometry because the linear weights were greatly negative or nonexistent. Following the works of Sonar [21], Harten and Chakravarthy [10], and Vankeirsbilck [26], we find [12] violated the principles of the spatial stencil selection algorithms. So a new layer of triangular cells was needed for constructing a fourth order finite volume WENO scheme [33] and three six-cell spatial stencils were added in the reconstruction procedures. The new fourth order finite volume WENO scheme in comparison with [12, 33] offers compactness and robustness and needs only five unequal sized spatial stencils for reconstructing unequal degree polynomials. The reconstruction procedures are similar to the third order finite volume WENO scheme.

The organization of the paper is as follows. In section 2, we emphasize the principle of constructing the new third order and fourth order finite volume WENO schemes in detail. In section 3, some numerical tests are presented to verify the simplicity and efficiency of these new WENO schemes. Concluding remarks are given in section 4.

2. Finite volume formulation for WENO schemes. We consider two-dimensional conservation laws (1.1) on triangular meshes and integrate (1.1) over the target cell $\triangle_0$ to obtain an integral formula as

$$\frac{d\bar{u}_0(t)}{dt} = -\frac{1}{|\triangle_0|}\int_{\partial\triangle_0} F\cdot\vec{n}ds, \tag{2.1}$$

where $\bar{u}_0(t) = \frac{1}{|\triangle_0|}\int_{\triangle_0} u(x,y,t)dxdy$, $F=(f,g)$, $\partial\triangle_0$ is the boundary of the target cell $\triangle_0$, $|\triangle_0|$ is the area of $\triangle_0$, and $\vec{n}$ denotes the outward unit normal to the boundary of $\triangle_0$. The line integrals in (2.1) are discretized by a two-point Gaussian integration formula [12] on every edge (for example, for a line segment with two endpoints (x_1,y_1) and (x_2,y_2), the two-point Gaussian quadrature points are $(x_{G_1},y_{G_1}) = ((\frac{1}{2}+\frac{\sqrt{3}}{6})x_1+(\frac{1}{2}-\frac{\sqrt{3}}{6})x_2, (\frac{1}{2}+\frac{\sqrt{3}}{6})y_1+(\frac{1}{2}-\frac{\sqrt{3}}{6})y_2)$ and $(x_{G_2},y_{G_2}) = ((\frac{1}{2}-\frac{\sqrt{3}}{6})x_1+(\frac{1}{2}+\frac{\sqrt{3}}{6})x_2, (\frac{1}{2}-\frac{\sqrt{3}}{6})y_1+(\frac{1}{2}+\frac{\sqrt{3}}{6})y_2)$, and the Gaussian quadrature weights are $\sigma_1=\sigma_2=\frac{1}{2}$):

$$\int_{\partial\triangle_0} F\cdot\vec{n}ds \approx \sum_{\ell\ell=1}^{3}|\partial\triangle_{0_{\ell\ell}}|\sum_{\ell=1}^{2}\sigma_\ell F(u(x_{G_{\ell\ell_\ell}},y_{G_{\ell\ell_\ell}},t))\cdot\vec{n}_{\ell\ell}. \tag{2.2}$$

And $F(u(x_{G_{\ell\ell_\ell}},y_{G_{\ell\ell_\ell}},t))\cdot\vec{n}_{\ell\ell}$, $\ell=1,2$, $\ell\ell=1,2,3$ are reformulated by numerical fluxes such as the Lax–Friedrichs flux

(2.3)

$$\begin{aligned} F(u(x_{G_{\ell\ell_\ell}},y_{G_{\ell\ell_\ell}},t))\cdot\vec{n}_{\ell\ell} \approx \frac{1}{2}\big[&(F(u^+(x_{G_{\ell\ell_\ell}},y_{G_{\ell\ell_\ell}},t))+F(u^-(x_{G_{\ell\ell_\ell}},y_{G_{\ell\ell_\ell}},t)))\cdot\vec{n}_{\ell\ell}\\ &-\alpha(u^+(x_{G_{\ell\ell_\ell}},y_{G_{\ell\ell_\ell}},t)-u^-(x_{G_{\ell\ell_\ell}},y_{G_{\ell\ell_\ell}},t))\big], \ell=1,2, \ell\ell=1,2,3, \end{aligned}$$

where α is taken as an upper bound for the eigenvalues of the Jacobian in the $\vec{n}_{\ell\ell}$ direction, u^+ and u^- are the approximations of the conservative values of u inside

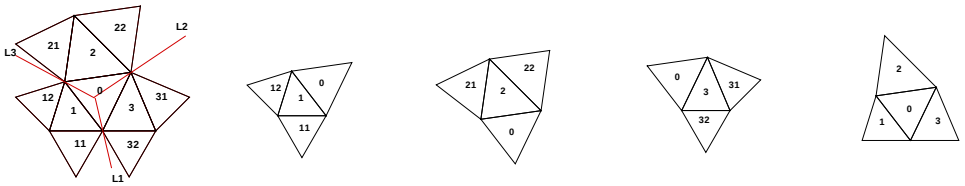

FIG. 2.1. *The first type of spatial stencils with three sectorial regions. From left to right:* T_1, T_2, T_3, T_4, T_5.

and outside of the target cell Δ_0 (inside of the neighboring triangular cell) at different Gaussian points, the reconstructions of u^+ and u^- will be described in the next subsections, and $|\partial\triangle_{0_{\ell\ell}}|, \ell\ell = 1, 2, 3$, are the length of the line segments. Then, (2.1) is approximated by the semidiscrete finite volume formula, and we can write the formula as

$$\frac{d\bar{u}_0(t)}{dt} = L(u). \tag{2.4}$$

2.1. Third order reconstruction. We then emphasize the spatial reconstruction procedures of a new third order finite volume WENO scheme on triangular meshes as follows. For simplicity, the reconstruction stencils are relabeled in Figure 2.1.

The reconstruction of function $u(x, y, t)$ at different Gaussian quadrature points $(x_{G_{\ell\ell_\ell}}, y_{G_{\ell\ell_\ell}})$, $\ell = 1, 2$, $\ell\ell = 1, 2, 3$, on the boundaries of the target cell $\triangle_0$ is narrated as follows. And we would like to omit the index of t in $u(x, y, t)$ in the following if it will not cause confusion.

Step 1.1. Select a big spatial stencil as $T_1 = \{\triangle_0, \triangle_1, \triangle_2, \triangle_3, \triangle_{11}, \triangle_{12}, \triangle_{21}, \triangle_{22}, \triangle_{31}, \triangle_{32}\}$ (see Figure 2.1). Then we construct a quadratic polynomial $p_1(x,y)\in span\{1, \frac{x-x_0}{|\triangle_0|^{\frac{1}{2}}}, \frac{y-y_0}{|\triangle_0|^{\frac{1}{2}}}, \frac{(x-x_0)^2}{|\triangle_0|}, \frac{(x-x_0)(y-y_0)}{|\triangle_0|}, \frac{(y-y_0)^2}{|\triangle_0|}\}$ on T_1 to obtain a third order approximation of conservative variable u, in which (x_0, y_0) is the barycenter of the target cell $\triangle_0$. Such a quadratic polynomial has the same cell average of u on the target cell $\triangle_0$ and matches the cell averages of u on the other triangles in the set $T_1 \setminus \{\triangle_0\}$ in a least square sense [12]:

$$\frac{1}{|\triangle_0|}\int_{\triangle_0} p_1(x, y)dxdy = \bar{u}_0, \quad \min \sum_{\ell\in A}\left(\frac{1}{|\triangle_\ell|}\int_{\triangle_\ell} p_1(x, y)dxdy - \bar{u}_\ell\right)^2, \tag{2.5}$$
$$A = \{1, 2, 3, 11, 12, 21, 22, 31, 32\}.$$

Step 1.2. After connecting the barycenter of the target cell Δ_0 with its three vertices, we define three lines L_1, L_2, and L_3 [17] (see Figure 2.1). These three lines partition the field into three sectors. Every sectorial stencil consists of several layers of neighboring cells of Δ_0 and the barycenters of these cells fall inside the sector. We need to reconstruct linear polynomials on such sectorial stencils [10, 21, 26]. Then we reconstruct four linear polynomials $p_\ell(x,y)\in span\{1, \frac{x-x_0}{|\triangle_0|^{\frac{1}{2}}}, \frac{y-y_0}{|\triangle_0|^{\frac{1}{2}}}\}$, $\ell = 2, \ldots, 5$ (three on sectorial stencils and one on central stencil, respectively), which satisfy the cell average of the conservative variable u on the target cell $\triangle_0$ and match the cell averages of u on the other triangles in a least square sense [12]. These four polynomials $p_\ell(x, y), \ell = 2, \ldots, 5$, are defined on small stencils $T_2 = \{\triangle_0, \triangle_1, \triangle_{11}, \triangle_{12}\}$, $T_3 = \{\triangle_0, \triangle_2, \triangle_{21}, \triangle_{22}\}$, $T_4 = \{\triangle_0, \triangle_3, \triangle_{31}, \triangle_{32}\}$, and $T_5 = \{\triangle_0, \triangle_1, \triangle_2, \triangle_3\}$, respectively. They satisfy

(2.6)
$$\frac{1}{|\triangle_0|}\int_{\triangle_0} p_\kappa(x,y)dxdy = \bar{u}_0, \min \sum_{\ell\in A_\kappa}\left(\frac{1}{|\triangle_\ell|}\int_{\triangle_\ell} p_\kappa(x,y)dxdy - \bar{u}_\ell\right)^2,$$
$$\kappa = 2,\ldots,5; A_2 = \{1,11,12\}, A_3 = \{2,21,22\}, A_4 = \{3,31,32\}, A_5 = \{1,2,3\}.$$

Remark 1. We could also design three more compact linear polynomials defined on different three-cell stencils ($T_2 = \{\triangle_0, \triangle_1, \triangle_2\}$, $T_3 = \{\triangle_0, \triangle_2, \triangle_3\}$, and $T_4 = \{\triangle_0, \triangle_3, \triangle_1\}$) in comparison with the linear polynomials defined on four-cell smaller stencils (see Figure 2.1). This reconstruction procedure violates the sectorial searching principle [10, 21, 26], which means such stencils $T_\ell, \ell = 2, 3, 4$, are not sectorial stencils because each barycenter of such triangles is not in the same sector, and it results in large truncation errors, spurious oscillations, or instabilities. Based on such analysis and the computation in the next section, we abandon the more compact three-cell stencils and fall back on the usage of the wider scale four-cell stencils.

Step 1.3. Define the values of linear weights. With a similar idea proposed by Levy, Puppo, and Russo [14, 15] for constructing CWENO schemes, we rewrite $p_1(x,y)$ as

$$p_1(x,y) = \gamma_1\left(\frac{1}{\gamma_1}p_1(x,y) - \sum_{\ell=2}^{5}\frac{\gamma_\ell}{\gamma_1}p_\ell(x,y)\right) + \sum_{\ell=2}^{5}\gamma_\ell p_\ell(x,y). \tag{2.7}$$

Note that (2.7) holds true for any choice of $\gamma_\ell, \ell = 1,\ldots,5$, with $\gamma_1 \neq 0$. In this paper, we would like to take positive linear weights with $\sum_{\ell=1}^{5}\gamma_\ell = 1$ and confirm $p_1(x,y)$ is the third order approximation to $u(x,y,t)$. Following the practice in [6, 29, 30, 34], for example, one type of such linear weights is defined as $\gamma_1 = 0.96$ and $\gamma_2 = \gamma_3 = \gamma_4 = \gamma_5 = 0.01$. However, some other robust WENO type schemes [6, 7, 8, 25] based on the artificial definition of the linear weights often degrade their optimal numerical accuracy.

Step 1.4. Compute the smoothness indicators, denoted by β_ℓ, $\ell = 1,\ldots,5$, which measure how smooth the functions $p_\ell(x,y)$, $\ell = 1,\ldots,5$, are in the target cell $\triangle_0$. The smaller these smoothness indicators, the smoother the functions are in the target cell. We use the same recipe for the smoothness indicators as in [12, 13]:

$$\beta_\ell = \sum_{|l|=1}^{r}\int_{\triangle_0}|\triangle_0|^{|l|-1}\left(\frac{\partial^{|l|}}{\partial x^{l_1}\partial y^{l_2}}p_\ell(x,y)\right)^2 dxdy,\ \ell = 1,\ldots,5, \tag{2.8}$$

where $l = (l_1, l_2)$, $|l| = l_1 + l_2$, and for $\ell = 1$, $r = 2$; for $\ell = 2,\ldots,5$, $r = 1$. We rewrite the polynomials as

$$p_\ell(x,y) = \sum_{|l|=0}^{r}\frac{(|\Delta_0|)^{\frac{|l|}{2}}}{l_1!l_2!}a_{l_1,l_2}^{(\ell)}\left(\frac{x-x_0}{|\Delta_0|^{\frac{1}{2}}}\right)^{l_1}\left(\frac{y-y_0}{|\Delta_0|^{\frac{1}{2}}}\right)^{l_2}, \ell = 1,\ldots,5. \tag{2.9}$$

Such coefficients $a_{l_1,l_2}^{(\ell)}$ of $p_\ell(x,y)$ are uniquely defined as solutions of the linear systems from (2.5) to (2.6) and the polynomials satisfy the accuracy conditions $u(x,y) - p_\ell(x,y) = O(|\Delta_0|^{\frac{|r|+1}{2}}), \ell = 1,\ldots,5$, which were proved in [21]. So the smoothness indicators in Taylor series at (x_0, y_0) are written as

$$\beta_1 = \left(\sum_{|l|=1}\left(\frac{\partial^{|l|}}{\partial x^{l_1}\partial y^{l_2}}u(x,y)|_{(x_0,y_0)}\right)^2\right)|\triangle_0|(1+O(|\triangle_0|)) = O(|\triangle_0|) \tag{2.10}$$

and

(2.11)
$$\beta_\ell = \left(\sum_{|l|=1} \left(\frac{\partial^{|l|}}{\partial x^{l_1} \partial y^{l_2}} u(x,y)|_{(x_0,y_0)} \right)^2 \right) |\triangle_0|(1 + O(|\triangle_0|^{\frac{1}{2}})) = O(|\triangle_0|),\ \ell = 2, \ldots, 5.$$

Step 1.5. Compute the nonlinear weights based on the linear weights and the smoothness indicators. For instance, we use τ [30, 31] for unequal degree polynomials defined on unequal sized spatial stencils which is simply defined as the absolute deference between $\beta_\ell, \ell = 1, \ldots, 5$, and is different from the formula specified in [2, 5] for equal degree polynomials on equal sized spatial stencils. The difference expansions in the Taylor series at (x_0, y_0) are

$$\beta_1 - \beta_\ell = O(|\triangle_0|^{\frac{3}{2}}),\ \ell = 2, \ldots, 5. \tag{2.12}$$

Then we get

$$\tau = \left(\frac{|\beta_1 - \beta_2| + |\beta_1 - \beta_3| + |\beta_1 - \beta_4| + |\beta_1 - \beta_5|}{4} \right)^2 = O(|\triangle_0|^3). \tag{2.13}$$

So the associated nonlinear weights are defined as

$$\omega_\ell = \frac{\bar{\omega}_\ell}{\sum_{\ell\ell=1}^{5} \bar{\omega}_{\ell\ell}}, \qquad \bar{\omega}_\ell = \gamma_\ell \left(1 + \frac{\tau}{\varepsilon + \beta_\ell} \right), \quad \ell = 1, \ldots, 5. \tag{2.14}$$

Here ε is a small positive number to avoid the denominator of (2.14) being zero. By the implementation of (2.13) in the smooth region, they satisfy

$$\frac{\tau}{\varepsilon + \beta_\ell} = O(|\triangle_0|^2),\ \ell = 1, \ldots, 5, \tag{2.15}$$

on the condition that $\varepsilon \ll \beta_\ell$. Therefore, the nonlinear weights ω_ℓ, $\ell = 1, \ldots, 5$, satisfy the order accuracy condition $\omega_\ell = \gamma_\ell + O(|\triangle_0|)$ [2, 5], providing the third order accuracy to the WENO schemes specified in [13, 22]. We denote $\varepsilon = 10^{-6}$ in all simulations in this paper.

Step 1.6. The final reconstruction polynomial for the approximation of $u(x, y)$ is given as

$$u(x,y) \approx Q(x,y) = \omega_1 \left(\frac{1}{\gamma_1} p_1(x,y) - \sum_{\kappa=2}^{5} \frac{\gamma_\kappa}{\gamma_1} p_\kappa(x,y) \right) + \sum_{\kappa=2}^{5} \omega_\kappa p_\kappa(x,y). \tag{2.16}$$

And the approximations can be given by

$$u^- \left(x_{G_{\ell\ell_\ell}}, y_{G_{\ell\ell_\ell}} \right) \approx Q \left(x_{G_{\ell\ell_\ell}}, y_{G_{\ell\ell_\ell}} \right),\ \ell = 1, 2, \ell\ell = 1, 2, 3, \tag{2.17}$$

at different Gaussian quadrature points on the boundaries of the target cell $\triangle_0$. As in [31], it is easy to prove that $Q(x, y)$ is the third order approximation to $u(x, y)$ when the solution is smooth.

Remark 2. By doing so, we only need to compute the nonlinear weights at all Gaussian quadrature points for one time and the nonlinear weights specified in [12] need to be computed for six times for all triangular cells in the computational field.

Step 1.7. Then the third order TVD Runge–Kutta time discretization method [23]

$$\begin{cases} u^{(1)} = u^n + \triangle t L(u^n), \\ u^{(2)} = \frac{3}{4}u^n + \frac{1}{4}u^{(1)} + \frac{1}{4}\triangle t L(u^{(1)}), \\ u^{n+1} = \frac{1}{3}u^n + \frac{2}{3}u^{(2)} + \frac{2}{3}\triangle t L(u^{(2)}) \end{cases} \tag{2.18}$$

is used to solve (2.4). Finally, we could obtain a fully discrete scheme in both space and time on triangular meshes.

Remark 3. If the triangular cells located inside the big central stencil T_1 are less than six because some cells merge with each other, we should use triangular cells in the next layer to reconstruct the quadratic polynomial in a least square sense [12]. There are two major differences between the spatial reconstruction procedures for the new third order finite volume WENO scheme and the classical third order finite volume WENO scheme [12]. The first is that one big central stencil, three small biased stencils, and one small central stencil are used in the paper, and one big central stencil and nine small biased stencils are used in [12]. The second is that the linear weights are independent of the meshes and can be any positive numbers with the only requirement that their summation is one, while the linear weights are dependent of both the meshes and where the value is reconstructed [12]. If the quadrature points are not chosen properly or the geometry of the computational meshes is rigid, the linear weights in [12] may become negative or even not exist at all [17, 20]. So the flowchart specified here for narrating the new third finite volume WENO scheme is very simple and robust in setting the linear weights at any quadrature points simultaneously keeping the third order accuracy in a smooth region without adjusting many parameters in constructing the numerical scheme.

2.2. Fourth order reconstruction. In this section, we only focus on the spatial procedures of a new fourth order finite volume WENO scheme on triangular meshes and other similar procedures are omitted for simplicity. The reconstruction of function $u(x, y, t)$ at different Gaussian quadrature points $(x_{G_{\ell\ell_\ell}}, y_{G_{\ell\ell_\ell}})$, $\ell = 1, 2$, $\ell\ell = 1, 2, 3$ on the boundaries of target cell $\triangle_0$ is narrated as follows.

Step 2.1. We first search the first neighboring triangles around the target cell Δ_0, let Δ_1, Δ_2, Δ_3 be its three neighboring triangles, and let Δ_{11}, Δ_{12} be the two neighboring triangles (other than Δ_0) of Δ_1, and so on to form a big central spatial stencil. Then we count the number of triangles in such stencil. If the number is 10 (see Figure 2.1), which means that there is no cell merged with the others, then we switch to Step 2.1.1. If the number is less than 10, for example, Figure 2.2, such a big stencil is not applicable for designing a fourth order spatial reconstruction, and then we need to search new neighboring triangles of the stencil sequentially until we

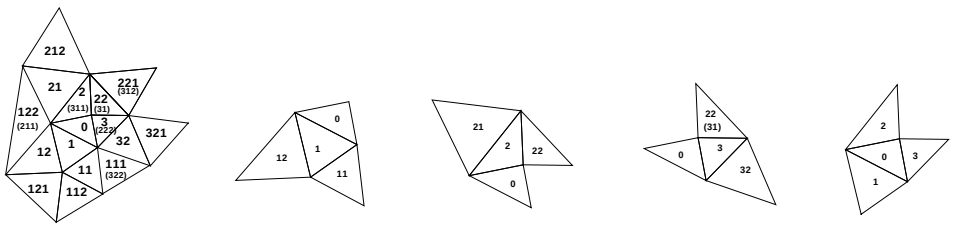

FIG. 2.2. *The second type of spatial stencils. From left to right:* T_1, T_2, T_3, T_4, T_5.

find at least a 10-cell spatial stencil and form a new stencil containing more than 10 triangles and switch to Step 2.1.2.

Step 2.1.1. Select the big stencil as $T_1 = \{\triangle_0, \triangle_1, \triangle_2, \triangle_3, \triangle_{11}, \triangle_{12}, \triangle_{21}, \triangle_{22}, \triangle_{31}, \triangle_{32}\}$ (see Figure 2.1). Then we construct a cubic polynomial $p_1(x,y) \in span\{1, \frac{x-x_0}{|\triangle_0|^{\frac{1}{2}}}, \frac{y-y_0}{|\triangle_0|^{\frac{1}{2}}}, \frac{(x-x_0)^2}{|\triangle_0|}, \frac{(x-x_0)(y-y_0)}{|\triangle_0|}, \frac{(y-y_0)^2}{|\triangle_0|}, \frac{(x-x_0)^3}{|\triangle_0|^{\frac{3}{2}}}, \frac{(x-x_0)^2(y-y_0)}{|\triangle_0|^{\frac{3}{2}}}, \frac{(x-x_0)(y-y_0)^2}{|\triangle_0|^{\frac{3}{2}}}, \frac{(y-y_0)^3}{|\triangle_0|^{\frac{3}{2}}}\}$ on T_1 to obtain a fourth order approximation of conservative variable u by requiring that it has the same cell averages of u on the target cell $\triangle_0$ and the other triangles:

$$\frac{1}{|\triangle_\ell|}\int_{\triangle_\ell} p_1(x,y)dxdy = \bar{u}_\ell, \ell = \{0,1,2,3,11,12,21,22,31,32\}. \tag{2.19}$$

Step 2.1.2. For example, as shown in Figure 2.2, we select a big central spatial stencil including at least 10 distinct triangles T_1=$\{\triangle_0, \triangle_1, \triangle_2, \triangle_3, \triangle_{11}, \triangle_{12}, \triangle_{21}, \triangle_{22}, \triangle_{31}, \triangle_{32}, \triangle_{111}, \triangle_{112}, \triangle_{121}, \triangle_{122}, \triangle_{211}, \triangle_{212}, \triangle_{221}, \triangle_{222}, \triangle_{311}, \triangle_{312}, \triangle_{321}, \triangle_{322}\}$. Then we can construct a cubic polynomial $p_1(x,y) \in span\{1, \frac{x-x_0}{|\triangle_0|^{\frac{1}{2}}}, \frac{y-y_0}{|\triangle_0|^{\frac{1}{2}}}, \frac{(x-x_0)^2}{|\triangle_0|}, \frac{(x-x_0)(y-y_0)}{|\triangle_0|}, \frac{(y-y_0)^2}{|\triangle_0|}, \frac{(x-x_0)^3}{|\triangle_0|^{\frac{3}{2}}}, \frac{(x-x_0)^2(y-y_0)}{|\triangle_0|^{\frac{3}{2}}}, \frac{(x-x_0)(y-y_0)^2}{|\triangle_0|^{\frac{3}{2}}}, \frac{(y-y_0)^3}{|\triangle_0|^{\frac{3}{2}}}\}$ on T_1 to obtain a fourth order approximation of conservative variable u by requiring that it has the same cell average of u on the target cell $\triangle_0$ and matches the cell averages of u on the other triangles in the set $T_1 \setminus \{\triangle_0\}$ in a least square sense [12]:

$$\frac{1}{|\triangle_0|}\int_{\triangle_0} p_1(x,y)dxdy = \bar{u}_0, \quad \min \sum_{\ell \in A}\left(\frac{1}{|\triangle_\ell|}\int_{\triangle_\ell} p_1(x,y)dxdy - \bar{u}_\ell\right)^2, \tag{2.20}$$

A=$\{1,2,3,11,12,21,22,31,32,111,112,121,122,211,212,221,222,311,312,321,322\}$.

Step 2.2. Construct four linear polynomials $p_\ell(x,y) \in span\{1, \frac{x-x_0}{|\triangle_0|^{\frac{1}{2}}}, \frac{y-y_0}{|\triangle_0|^{\frac{1}{2}}}\}$, $\ell = 2,\ldots,5$, which satisfy the cell average of the conservative variable u on the target cell $\triangle_0$ and match the cell averages of u on the other triangles in a least square sense [12]. They are identical to the formulas specified in Step 1.2.

Remark 4. To obtain a fourth order numerical approximation at any quadrature points inside the target cell Δ_0, we construct a cubic polynomial based on the big central spatial stencil (the target cell Δ_0 is on the center of the stencil) to cause fewer truncation errors than on the big biased spatial stencil (the target cell Δ_0 is not on the center of the spatial stencil). In this new spatial reconstruction procedure, we do not need to study all possible cases of such a spatial stencil (the big stencil T_1 has nothing to do with each of the small stencils $T_\ell, \ell = 2,\ldots,5$, because the linear weights in this paper do not reveal the relationship between the polynomials defined on such stencils at different quadrature points and are artificially set). On the contrary, it is very crucial and needs to be discussed in detail for many WENO schemes [12, 20, 28].

Remark 5. We construct a cubic polynomial $p_1(x,y)$ by requiring that it have the same cell averages on triangular cells including $\triangle_0$ and its neighboring three cells and their next at least six neighboring cells in T_1. If one cubic polynomial and nine linear polynomials in [12] are reconstructed, the linear systems for solving the linear weights at different quadrature points are grossly overdetermined and insoluble. So the number of the spatial stencils used in designing the new fourth order finite volume WENO scheme on triangular meshes is smaller. To remedy this drawback, Hu and

Shu [12] used a cubic polynomial based on the cell averages defined on a 10-cell spatial stencil and six quadratic polynomials based on the cell averages defined on six six-cell smaller spatial stencils. Then they computed linear systems to obtain the linear weights at different quadrature points. This procedure is very essential for the second type of finite volume WENO schemes to obtain their optimal order of accuracy in a smooth region on the condition that the meshes do not distort too much; otherwise, we should apply the technique of treating negative linear weights in [20] or the technique of achieving a robust unstructured finite volume WENO reconstruction on complex mesh geometries [17].

Step 2.3. Set the linear weights.

Step 2.4. Compute the smoothness indicators β_ℓ, $\ell = 1, \ldots, 5$ [12, 13], by the application of (2.8). Their expansions in Taylor series at (x_0, y_0) are

$$\beta_1 = \left(\sum_{|l|=1} \left(\frac{\partial^{|l|}}{\partial x^{l_1} \partial y^{l_2}} u(x,y)|_{(x_0,y_0)} \right)^2 \right) |\triangle_0| \left(1 + O\left(|\triangle_0|^{\frac{3}{2}} \right) \right) = O(|\triangle_0|) \tag{2.21}$$

and (2.11).

Step 2.5. Compute the nonlinear weights based on the linear weights and the smoothness indicators. For instance, we use τ [30, 31], which is simply defined as the absolute deference between β_1, β_2, β_3, β_4, and β_5, and the difference expansions in the Taylor series at (x_0, y_0) are

$$\beta_1 - \beta_\ell = O\left(|\triangle_0|^{\frac{3}{2}} \right), \ \ell = 2, \ldots, 5. \tag{2.22}$$

So it satisfies

$$\tau = \left(\frac{|\beta_1 - \beta_2| + |\beta_1 - \beta_3| + |\beta_1 - \beta_4| + |\beta_1 - \beta_5|}{4} \right)^2 = O(|\triangle_0|^3). \tag{2.23}$$

Then the associate nonlinear weights are defined as that specified in Step 1.5. By the performance of (2.23) in a smooth region, they satisfy

$$\frac{\tau}{\varepsilon + \beta_\ell} = O(|\triangle_0|^2), \ \ \ell = 1, \ldots, 5, \tag{2.24}$$

on the condition that $\varepsilon \ll \beta_\ell$. Therefore, the nonlinear weights ω_ℓ, $\ell = 1, \ldots, 5$, satisfy the order accuracy condition $\omega_\ell = \gamma_\ell + O(|\triangle_0|^{\frac{3}{2}})$ [2, 5], providing the fourth order accuracy to the WENO scheme [13, 22].

Step 2.6. The new final reconstruction formulations of conservative values $u(x, y, t)$ at different Gaussian quadrature points $(x_{G_{\ell\ell_\ell}}, y_{G_{\ell\ell_\ell}})$, $\ell = 1, 2$, $\ell\ell = 1, 2, 3$, on the boundaries of the target cell $\triangle_0$ are given by (2.16) and (2.17). As shown in (2.17), we compute the nonlinear weights for all quadrature points only once in comparison with six times in [12] for every target cell Δ_0.

Step 2.7. Then the third order TVD Runge–Kutta time discretization method [23] (2.18) is applied for solving the ODE (2.4) on triangular meshes.

Remark 6. In [21], Sonar pointed out the constructional principle of essentially nonoscillatory finite volume approximations to compressible fluid dynamics on triangular meshes. He gave a new narration of the applicable methodologies for the stencil selection principle to recover polynomials of arbitrary degree. Harten and Chakravarthy [10] proposed a sectorial search in order to keep the number of possible stencils small. Sectorial search was also used by Vankeirsbilck [26] in connection

with a box method. So it is useful to search for a bigger spatial stencil including 16 triangular cells [33] and reconstruct a cubic polynomial in a least square sense and 9 quadratic polynomials, and calculate linear systems for solving linear weights at different quadrature points. This analysis partly explains the truth about why there is no fourth order WENO scheme for the simulation of a Mach 3 wind tunnel with a step problem in [12] because of the violation of the associated principles. Generally speaking, it is the first time for us to design a fourth order finite volume WENO scheme by usage of the cell averages on only 10 distinct triangular cells (see Figure 2.1) to formulate five unequal degree polynomials for high order approximations at any points inside the target cell robustly without taking into account the good or bad quality of the triangular meshes.

3. Numerical results. In this section we provide numerical examples to demonstrate the performance of the new third order and fourth order finite volume WENO schemes on triangular meshes described in the previous section. For systems of the compressible Euler equations, all of the reconstructions are performed in the local characteristic directions to avoid spurious oscillations. The CFL number is 0.6. For the temporal discretization, the third order TVD Runge–Kutta time discretization method [23] is used here for all examples. Only for the accuracy tests, we set the time step as $\Delta t = \min_\ell(|\Delta_\ell|^{\frac{1}{2}})^{\frac{\kappa}{3}}$, and $\kappa = 3$ (for the third order WENO scheme) or $\kappa = 4$ (for the fourth order WENO scheme) to confirm that spatial error dominates. Otherwise, we recover $\kappa = 3$ for other examples in this paper. For the purpose of evaluating whether the random choice of the linear weights would pollute the optimal order of these new WENO schemes, we set four different types of linear weights in the numerical accuracy cases as (1) $\gamma_1 = 0.96$ and $\gamma_2 = \gamma_3 = \gamma_4 = \gamma_5 = 0.01$; (2) $\gamma_1 = \gamma_2 = \gamma_3 = \gamma_4 = \gamma_5 = 0.2$; (3) $\gamma_1 = 0.01$ and $\gamma_2 = \gamma_3 = \gamma_4 = \gamma_5 = 0.2475$; (4) $\gamma_1 = \gamma_2 = \gamma_3 = \gamma_4 = 0.01$ and $\gamma_5 = 0.96$. Then we use the first two types of linear weights from Examples 3.3 to 3.7 and apply the first type of linear weights for the latter examples, unless specified otherwise.

Example 3.1. We solve the following Burgers' equation in two dimensions:

$$\mu_t + \left(\frac{\mu^2}{2}\right)_x + \left(\frac{\mu^2}{2}\right)_y = 0, \quad (x, y) \in [-2, 2] \times [-2, 2], \tag{3.1}$$

with the initial condition $\mu(x, y, 0) = 0.5 + \sin(\pi(x + y)/2)$ and periodic boundary conditions in both directions. We compute the solution up to $t = 0.5/\pi$. For this test case, two types of the computational meshes denoted as mesh I (boundary points are uniformly distributed) and mesh II (boundary points are not uniformly distributed) are used. The samples of these meshes are shown in Figure 3.1. The errors and numerical orders of accuracy for the third order and fourth order finite volume WENO schemes are shown in Figure 3.2. The new finite volume WENO schemes can keep the designed order of accuracy with different sets of linear weights in this classical scalar nonlinear accuracy test case.

Example 3.2. We solve the two-dimensional Euler equations

$$\frac{\partial}{\partial t}\begin{pmatrix} \rho \\ \rho\mu \\ \rho\nu \\ E \end{pmatrix} + \frac{\partial}{\partial x}\begin{pmatrix} \rho\mu \\ \rho\mu^2 + p \\ \rho\mu\nu \\ \mu(E + p) \end{pmatrix} + \frac{\partial}{\partial y}\begin{pmatrix} \rho\nu \\ \rho\nu\mu \\ \rho\nu^2 + p \\ \nu(E + p) \end{pmatrix} = 0, (x, y) \in [0, 2] \times [0, 2], \tag{3.2}$$

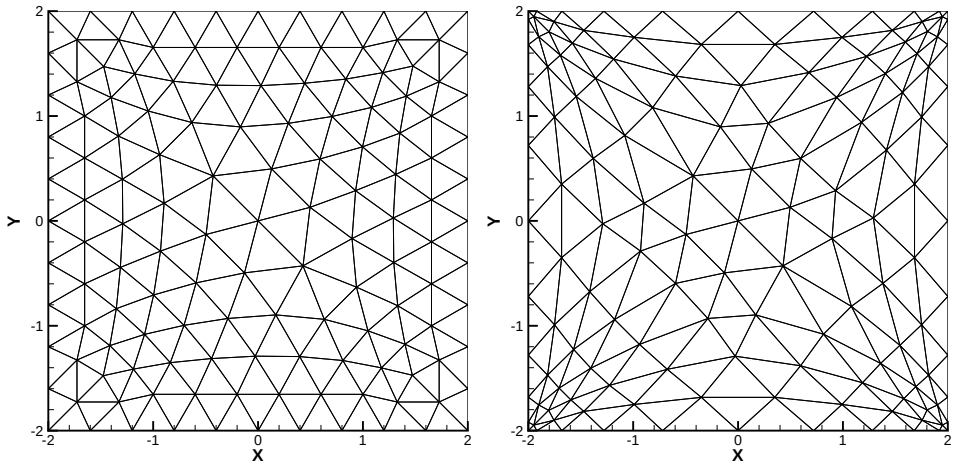

FIG. 3.1. *Burgers' equation. Sample mesh* I *(left), where mesh points are uniformly distributed on the boundary. Sample mesh* II *(right), where mesh points are not uniformly distributed on the boundary.*

where ρ is density; μ and ν are the velocities in the x and y directions, respectively; E is total energy; and p is pressure, which is related to the total energy by $E = p/(\gamma-1) + \frac{1}{2}\rho(\mu^2+\nu^2)$ with $\gamma = 1.4$. The initial conditions are $\rho(x,y,0) = 1+0.2\sin(\pi(x+y))$, $\mu(x,y,0) = 0.5$, $\nu(x,y,0) = 0.5$, and $p(x,y,0) = 1$. Periodic boundary conditions are applied in both directions. The exact solution is $\rho(x,y,t) = 1+0.2\sin(\pi(x+y-t))$. The solution is computed up to $t = 2$. For this test case, the sample meshes are similar to Figure 3.1 except for a different computational domain. The errors and numerical orders of the WENO schemes are shown in Figure 3.3. We can see that these schemes could keep the theoretical order of accuracy with different artificially chosen linear weights.

Remark 7. The finite volume WENO schemes obtain high order accuracy in the smooth region with different types of linear weights. We observe the WENO schemes with the first type of linear weights could get least L^1 and L^∞ truncation errors for such examples.

Example 3.3. We solve the two-dimensional Euler equations (3.2) with the Riemann initial condition for the Lax problem:

$$(\rho,\mu,\nu,p)^T = \begin{cases} (0.445, 0.698, 0, 3.528)^T, & x \in [-0.5, 0), \\ (0.5, 0, 0, 0.571)^T, & x \in [0, 0.5]. \end{cases} \tag{3.3}$$

The final time is $t = 0.16$. The computational domain is $[-0.5, 0.5] \times [-5\Delta x, 5\Delta x]$ which is with a triangulation of 101 vertices in the x direction and 11 vertices in the y direction. The periodic boundary condition is applied in the y direction. The results and zoomed-in pictures for two different schemes are shown in Figure 3.4. We observe that the computational results obtained by the associated WENO schemes are good.

Example 3.4. We solve the two dimensional Euler equations (3.2) with Riemann initial condition for the Sod problem:

$$(\rho,\mu,\nu,p)^T = \begin{cases} (1, 0, 0, 2.5)^T, & x \in [-5, 0), \\ (0.125, 0, 0, 0.25)^T, & x \in [0, 5]. \end{cases} \tag{3.4}$$

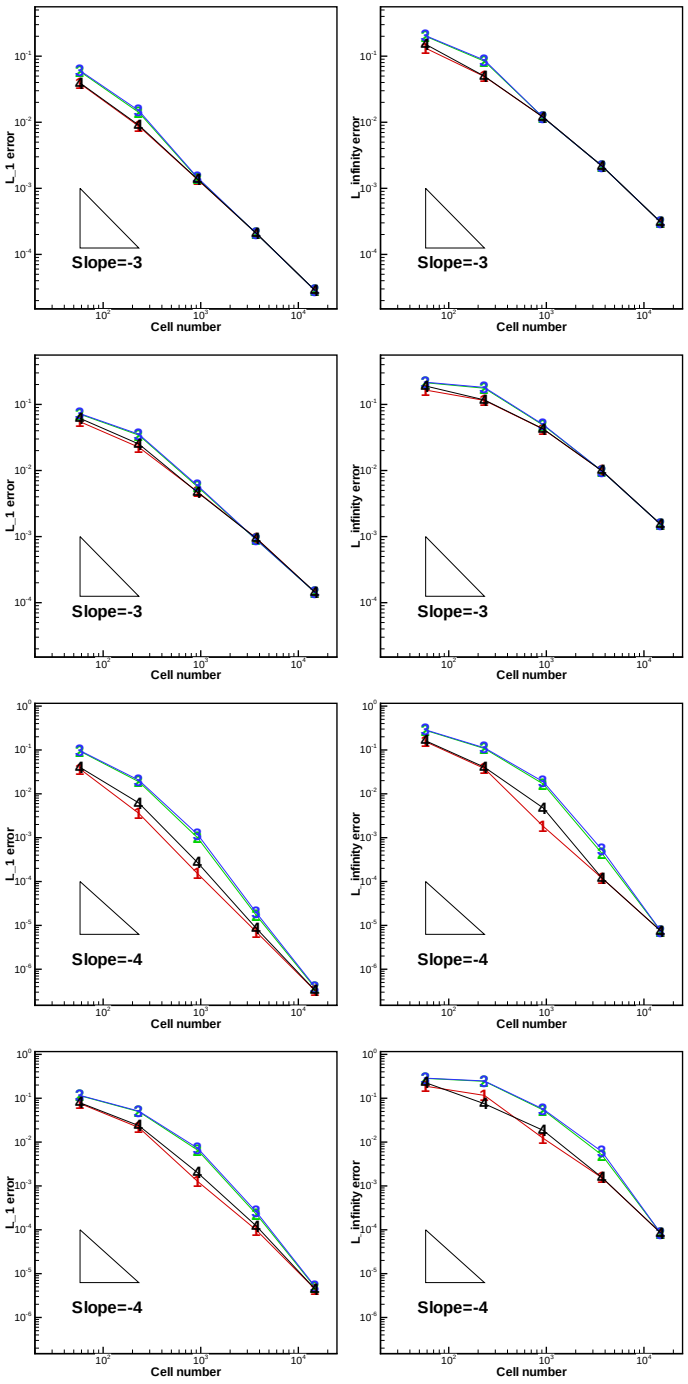

FIG. 3.2. *Burgers' equation.* $T=\frac{0.5}{\pi}$. *From left to right:* L^1 *error,* L^∞ *error. Number signs and a solid line denote the results of WENO schemes with different linear weights* (1), (2), (3), *and* (4). *From top to bottom: the third order WENO scheme with and without uniformly distributed mesh points on the boundary, and the fourth order WENO scheme with and without uniformly distributed mesh points on the boundary.*

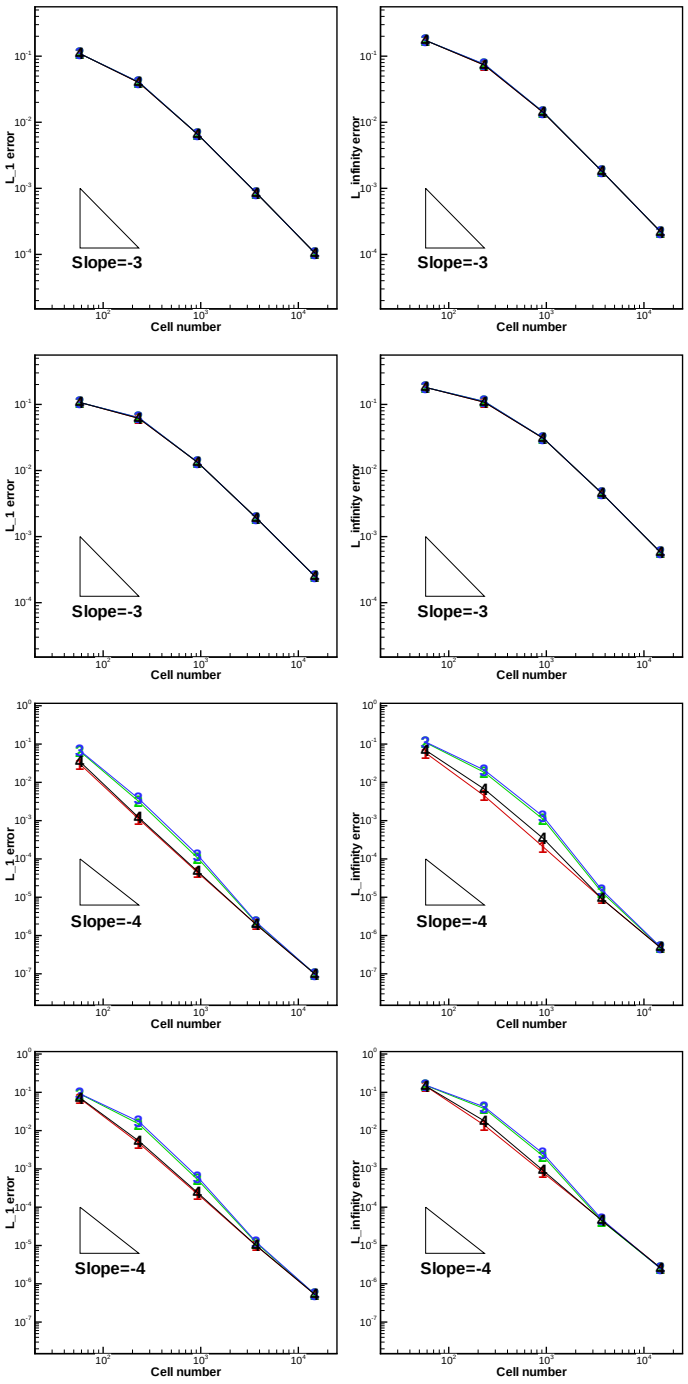

FIG. 3.3. *Two-dimensional Euler equations.* $T = 2$. *From left to right:* L^1 *error,* L^∞ *error. Number signs and a solid line denote the results of WENO schemes with different linear weights* (1), (2), (3), *and* (4). *From top to bottom: the third order WENO scheme with and without uniformly distributed mesh points on the boundary, and the fourth order WENO scheme with and without uniformly distributed mesh points on the boundary.*

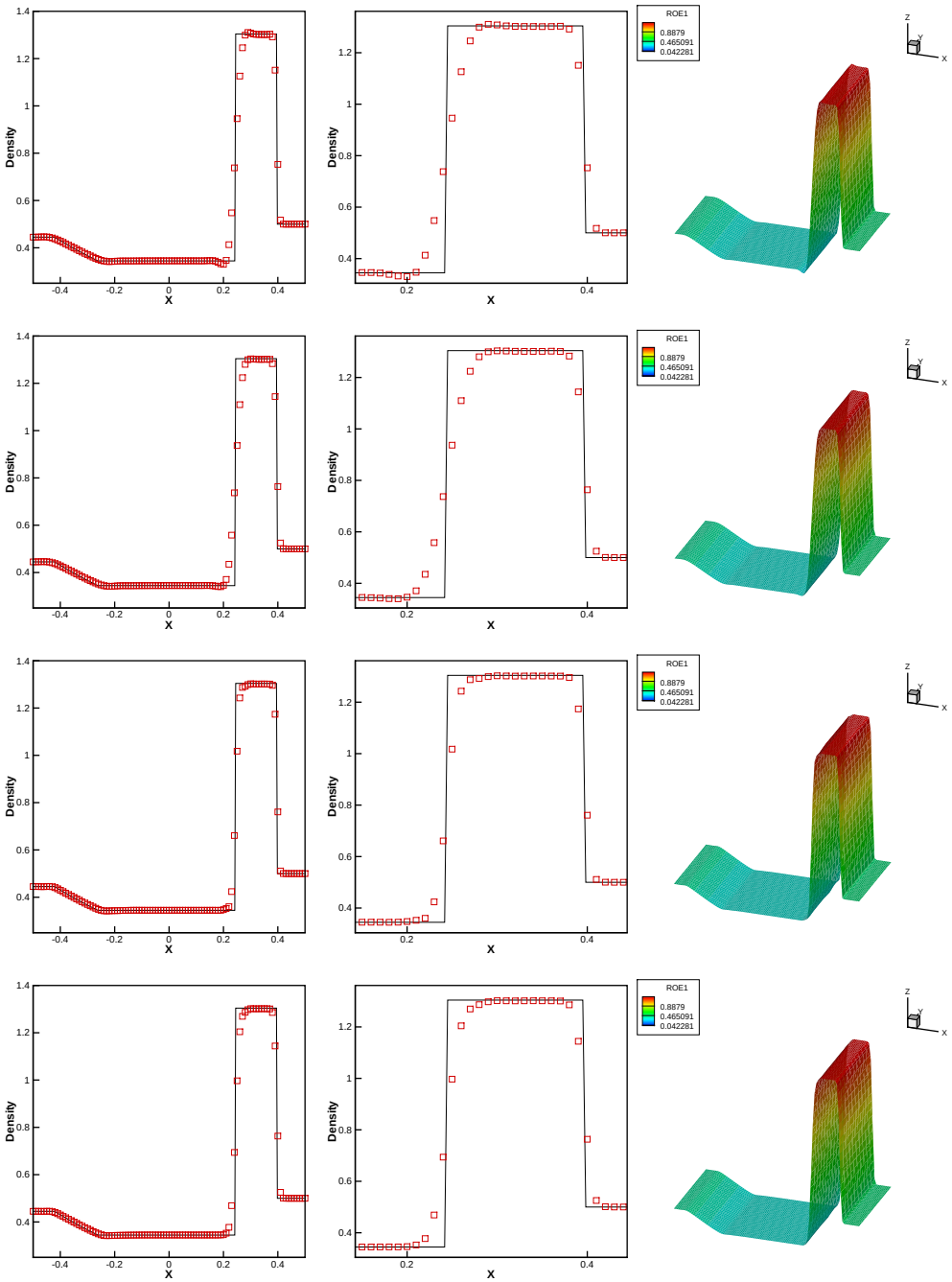

FIG. 3.4. *The Lax problem.* $T = 0.16$. *From left to right: density; density zoomed in; three-dimensional density surface. Solid line: the exact solution; squares: the results of WENO schemes. From top to bottom: the third order WENO* (1) *scheme; the third order WENO* (2) *scheme; the fourth order WENO* (1) *scheme; the fourth order WENO* (2) *scheme. The mesh points on the boundary are uniformly distributed with cell length* $h = 1/100$.

The final time is $t = 2$. The computational domain is $[-5, 5] \times [-5\Delta x, 5\Delta x]$ which is with a triangulation of 101 vertices in the x direction and 11 vertices in the y direction. The periodic boundary condition is applied in the y direction. The results and zoomed-in pictures for associated schemes are shown in Figure 3.5. The numerical results computed by the WENO schemes are good for this one-dimensional test example.

Example 3.5. A higher order scheme would show its advantage when the solution contains both shocks and complex smooth region structures. A typical example for this is the problem of shock interaction with entropy waves [22]. We solve the Euler equations (3.2) with a moving Mach = 3 shock interacting with sine waves in density in the x direction: $(\rho, \mu, \nu, p)^T = (3.857143, 2.629369, 0, 10.333333)^T$ for $x \in [-5, -4)$; $(\rho, \mu, \nu, p)^T = (1 + 0.2\sin(5x), 0, 0, 1)^T$ for $x \in [-4, 5]$. The computational domain is $[-5, 5] \times [-5\Delta x, 5\Delta x]$ which is with a triangulation of 401 vertices in the x direction and 11 vertices in the y direction. The periodic boundary condition is applied in the y direction. The computed density ρ is plotted at $t = 1.8$ against the referenced "exact" solution which is a converged solution computed by the finite difference fifth order WENO scheme [13] with 2000 grid points in Figure 3.6. The new type of finite volume WENO schemes could get good resolution for this benchmark example.

Example 3.6. We now consider the interaction of two blast waves. The initial conditions are

$$(\rho, \mu, \nu, p)^T = \begin{cases} (1, 0, 0, 10^3)^T, & 0 < x < 0.1, \\ (1, 0, 0, 10^{-2})^T, & 0.1 < x < 0.9, \\ (1, 0, 0, 10^2)^T, & 0.9 < x < 1. \end{cases} \tag{3.5}$$

The computed density ρ is plotted at $t = 0.038$ against the reference "exact" solution which is a converged solution computed by the finite difference fifth order WENO scheme [13] with 2000 grid points. The computational domain is $[0, 1] \times [-5\Delta x, 5\Delta x]$ which is with a triangulation of 401 vertices in the x direction and 11 vertices in the y direction. The periodic boundary condition is applied in the y direction. The results and zoomed-in pictures for different schemes are shown in Figure 3.7. The new WENO schemes could get good performance as before.

Example 3.7. We solve the same two-dimensional Burgers' equation (3.1) with the same initial condition $\mu(x, y, 0) = 0.5 + \sin(\pi(x + y)/2)$, except that the results are plotted at $t = 1.5/\pi$ when a shock has already appeared in the computational domain. The solutions are shown in Figures 3.8 and 3.9. We can see that the new schemes give nonoscillatory shock transitions nearby discontinuities sharply without considering the mesh's geometry which is crucial to confine associated nonnegative linear weights [20].

Remark 8. The finite volume WENO schemes could obtain sharp shock transitions with different types of linear weights. But we also find the schemes with the first type of linear weights could get better numerical resolutions. Thereafter, we only simulate the latter examples by the application of the new WENO schemes with the first type of linear weights for simplicity.

Example 3.8. *Double Mach reflection problem.* This model problem is originally from [27]. We solve the Euler equations (3.2) in a computational field $[0, 4] \times [0, 1]$. The reflection boundary condition is used at the wall, which for the rest of the bottom boundary (the part from $x = 0$ to $x = \frac{1}{6}$), the exact postshock condition is imposed.

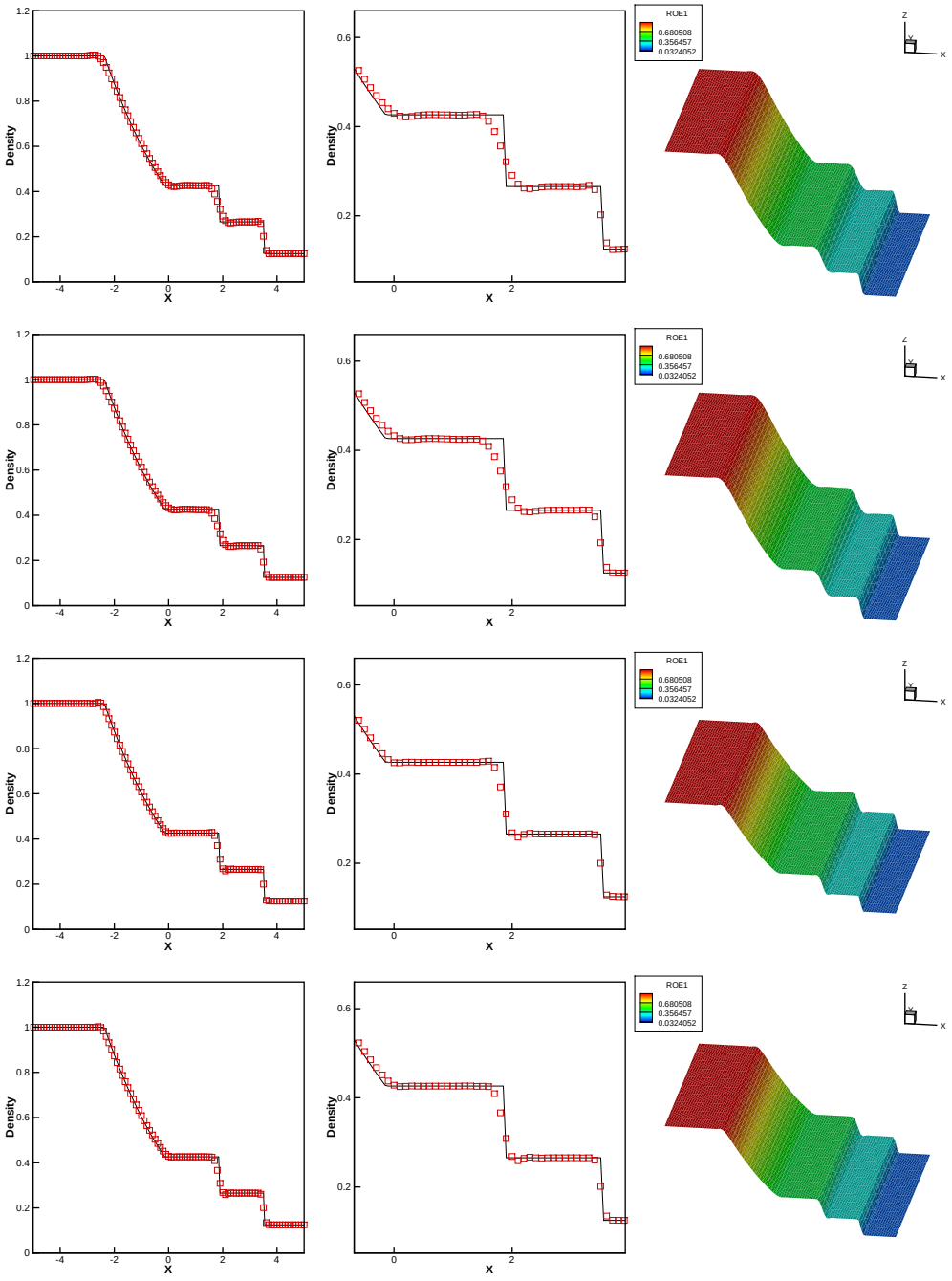

FIG. 3.5. *The Sod problem.* $T = 2$. *From left to right: density; density zoomed in; three-dimensional density surface. Solid line: the exact solution; squares: the results of WENO schemes. From top to bottom: the third order WENO* (1) *scheme; the third order WENO* (2) *scheme; the fourth order WENO* (1) *scheme; the fourth order WENO* (2) *scheme. The mesh points on the boundary are uniformly distributed with cell length* $h = 1/100$.

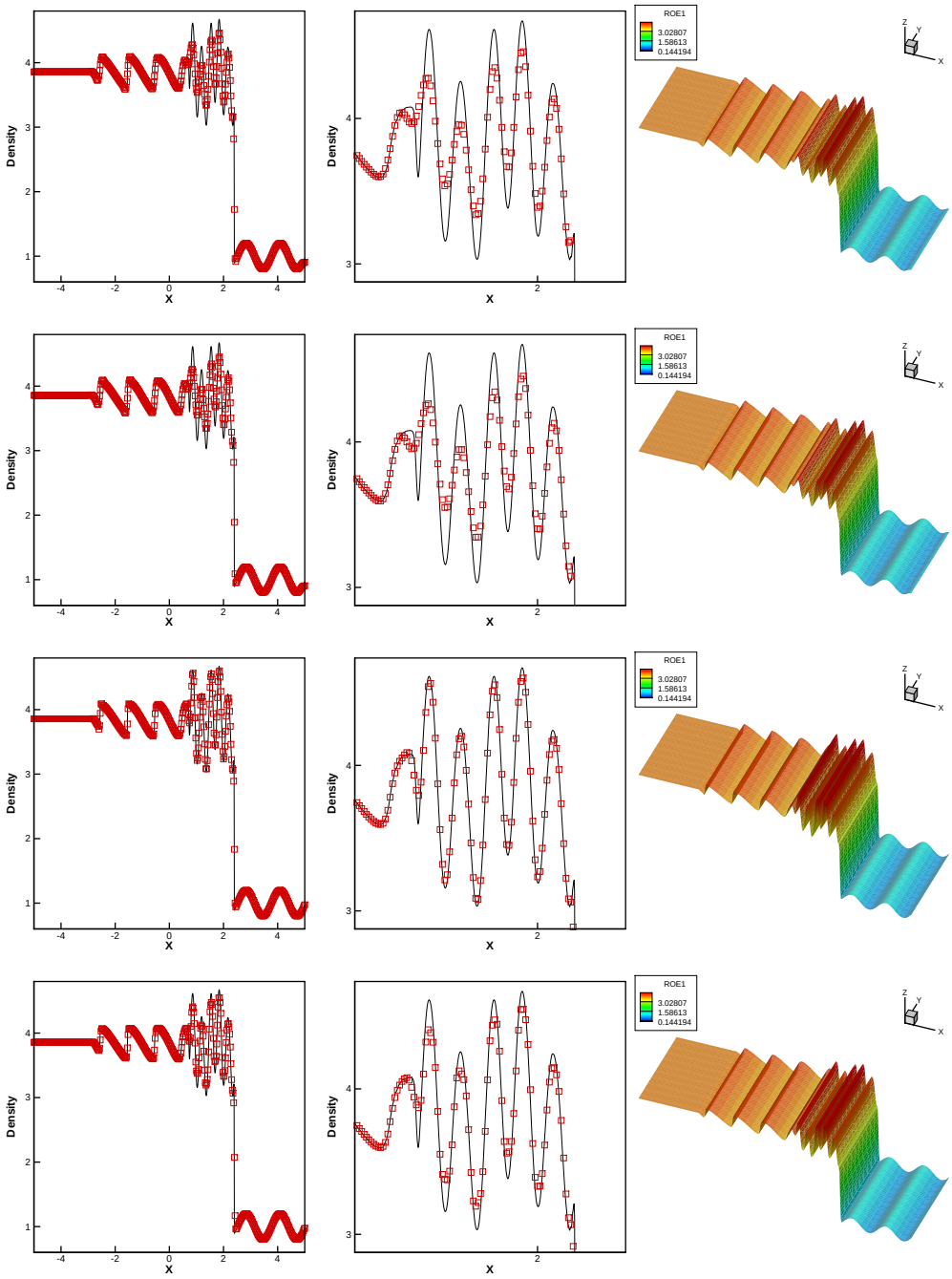

FIG. 3.6. *The shock density wave interaction problem.* $T = 1.8$. *From left to right: density; density zoomed in; three-dimensional density surface. Solid line: the exact solution; squares: the results of WENO schemes. From top to bottom: the third order WENO* (1) *scheme; the third order WENO* (2) *scheme; the fourth order WENO* (1) *scheme; the fourth order WENO* (2) *scheme. The mesh points on the boundary are uniformly distributed with cell length* $h = 1/400$.

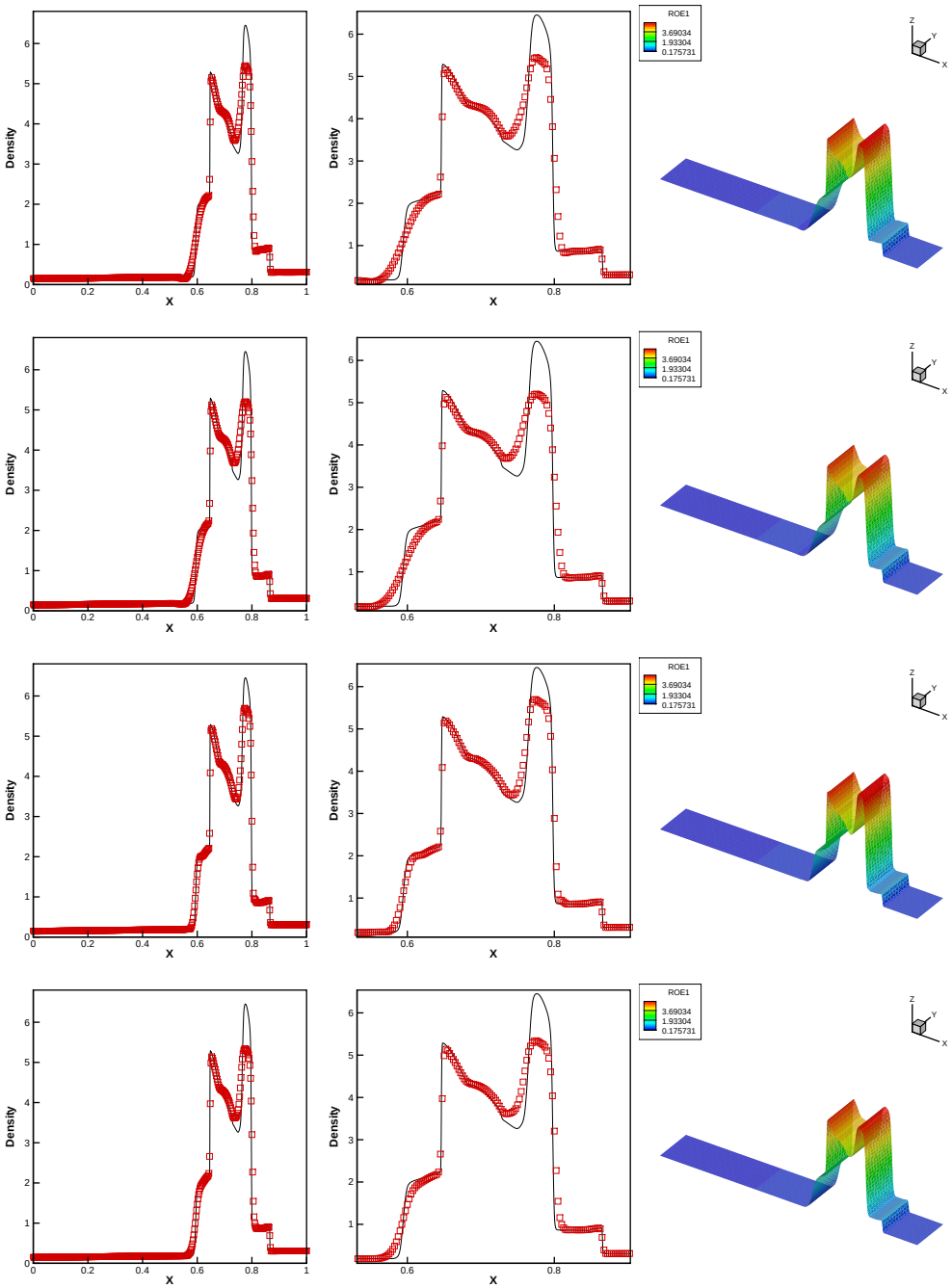

FIG. 3.7. *The blast wave problem.* $T = 0.038$. *From left to right: density; density zoomed in; three-dimensional density surface. Solid line: the exact solution; squares: the results of WENO schemes. From top to bottom: the third order WENO* (1) *scheme; the third order WENO* (2) *scheme; the fourth order WENO* (1) *scheme; the fourth order WENO* (2) *scheme. The mesh points on the boundary are uniformly distributed with cell length* $h = 1/400$.

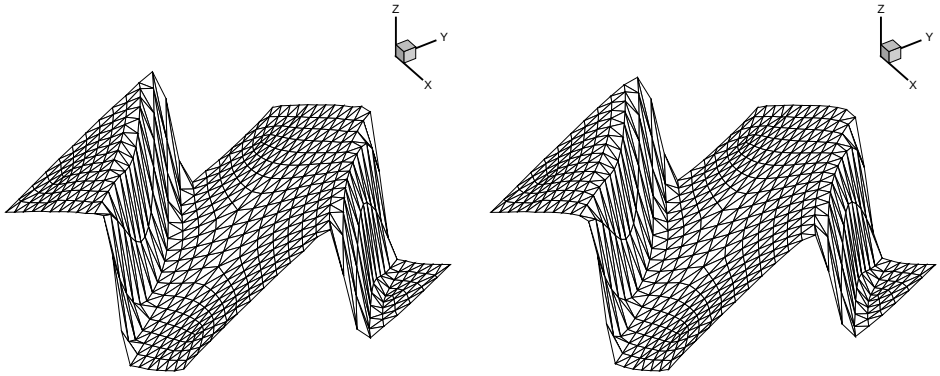

FIG. 3.8. *Burgers' equation.* $T = 1.5/\pi$. *The surface of the solution. Left: the third order WENO* (1) *scheme; right: the fourth order WENO* (1) *scheme. The mesh points on the boundary are uniformly distributed with cell length* $h = 4/20$.

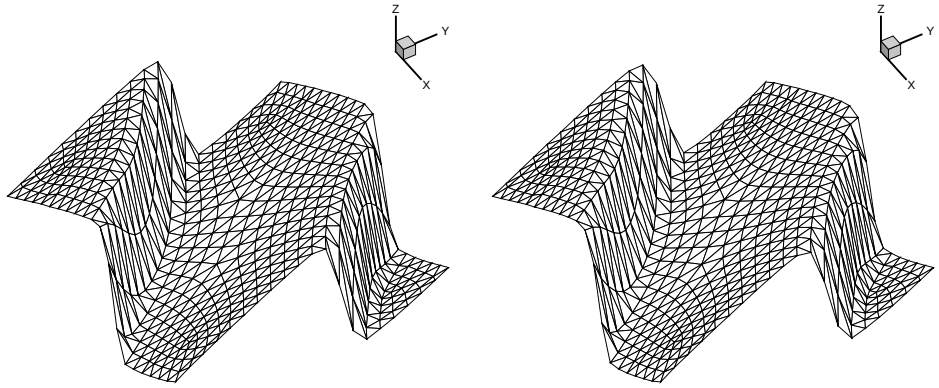

FIG. 3.9. *Burgers' equation.* $T = 1.5/\pi$. *The surface of the solution. Left: the third order WENO* (2) *scheme; right: the fourth order WENO* (2) *scheme. The mesh points on the boundary are uniformly distributed with cell length* $h = 4/20$.

At the top boundary is the exact motion of the Mach 10 shock. The numerical results are shown at $t = 0.2$. Two different orders of finite volume WENO schemes are used in this numerical experiment. A sample mesh coarser than what is used is shown in Figure 3.10. The computing mesh has 392693 points and 708576 cells inside of the field. And 12 cells among the total 708576 cells (the percentage is 0.00169%) are needed to use three layers of the cells for the lack of 10 distinct triangular cells by applying two layers in designing the fourth order WENO scheme. The simulation results are shown in Figure 3.11. The zoomed-in pictures around the double Mach stem to show more details are given in Figure 3.12. We could get perfect results once again.

Example 3.9. *A Mach* 3 *wind tunnel with a step.* This model problem is also

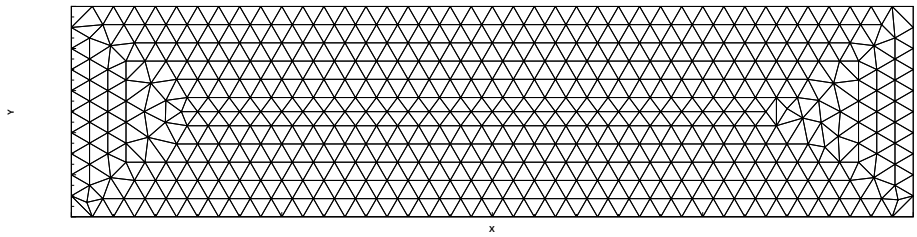

FIG. 3.10. *Double Mach reflection problem. Sample mesh.*

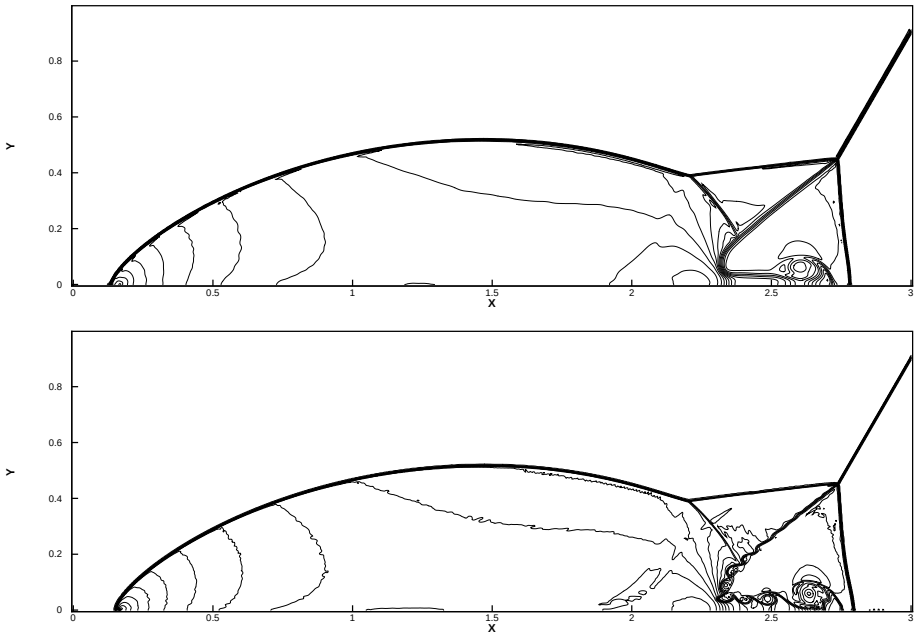

FIG. 3.11. *Double Mach reflection problem.* 30 *equally spaced density contours from* 1.5 *to* 22.7. *Top: the third order WENO* (1) *scheme; bottom: the fourth order WENO* (1) *scheme. The mesh points on the boundary are uniformly distributed with cell length* $h = 1/320$.

originally from [27]. The setup of the problem is as follows. The wind tunnel is 1 length unit wide and 3 length units long. The step is 0.2 length units high and is located 0.6 length units from the left-hand end of the tunnel. The problem is initialized by a right-going Mach 3 flow. Reflective boundary conditions are applied along the wall of the tunnel and inflow/outflow boundary conditions are applied at the entrance/exit. There is a singularity at the corner of the step. However, we do not modify our schemes or refine the mesh near the corner, in order to test the performance of our schemes for such singularity. The results are shown at $t = 4$. A sample mesh coarser than what is used is shown in Figure 3.13. The computing mesh has 108331 points and 149864 cells inside the field. And 44 cells

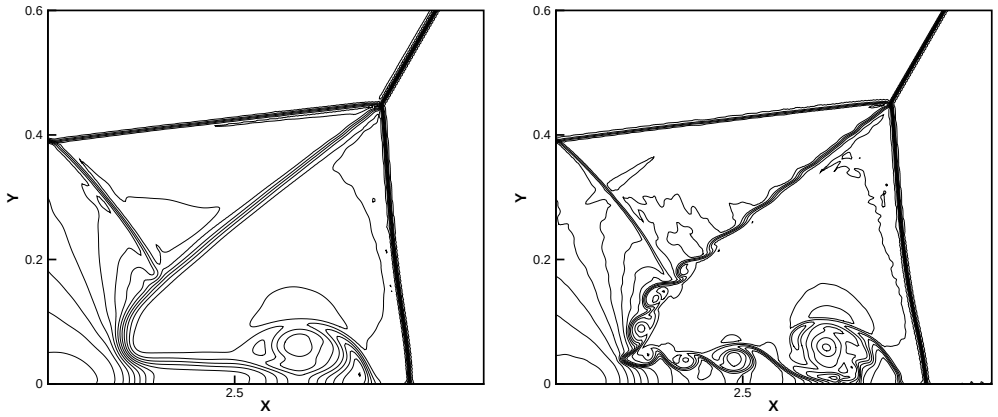

FIG. 3.12. *Double Mach reflection problem. Zoomed-in pictures around the Mach stem.* 30 *equally spaced density contours from* 1.5 *to* 22.7. *Left: the third order WENO* (1) *scheme; right: the fourth order WENO* (1) *scheme. The mesh points on the boundary are uniformly distributed with cell length* $h = 1/320$.

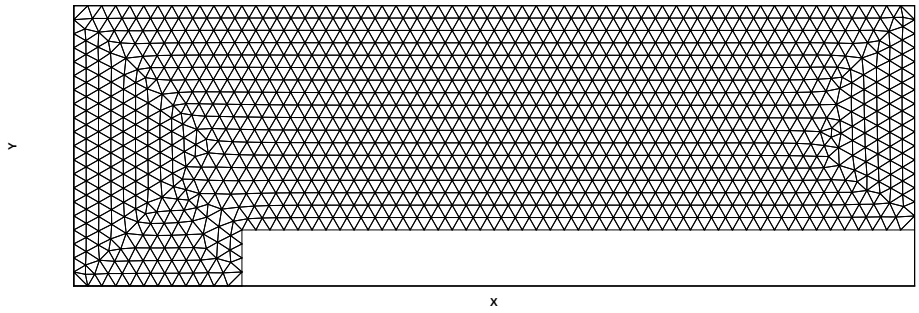

FIG. 3.13. *Forward step problem. Sample mesh.*

among the total cells (the percentage is 0.029%) are needed to use three layers of the neighboring cells to propose the fourth order WENO scheme. Then the results of 30 equally spaced density contours from 0.32 to 6.15 computed by the third order and fourth order WENO schemes are shown in Figure 3.14. We can clearly observe that the fourth order scheme gives better resolution than the third order scheme, especially for the resolution of the physical instability and roll-up of the contact line.

Example 3.10. We consider inviscid Euler transonic flow past a single NACA0012 airfoil configuration [21] with Mach number $M_\infty = 0.8$ and angle of attack $\alpha = 1.25°$ and with $M_\infty = 0.85$ and angle of attack $\alpha = 1°$. The computational domain is $[-15, 15] \times [-15, 15]$. The computational mesh used in the example is shown in Figure 3.15, which consists of 9340 triangles, and the minimum and maximum diameters of the circumcircle of all triangles are 0.0031 and 1.4188, respectively. The new WENO schemes are used in the simulations. Of the total 9340 cells, 336 (the percentage is 3.59%) are needed to use three layers of triangular cells to propose the fourth order

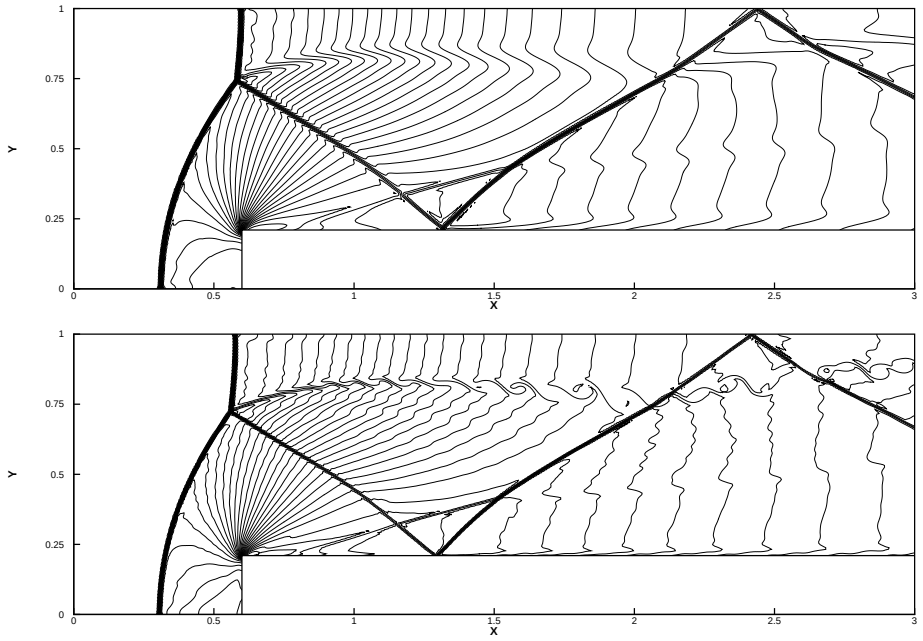

FIG. 3.14. *Forward step problem.* 30 *equally spaced density contours from* 0.32 *to* 6.15. *Top: the third order WENO* (1) *scheme; bottom: the fourth order WENO* (1) *scheme. The mesh points on the boundary are uniformly distributed with cell length* $h = 1/160$.

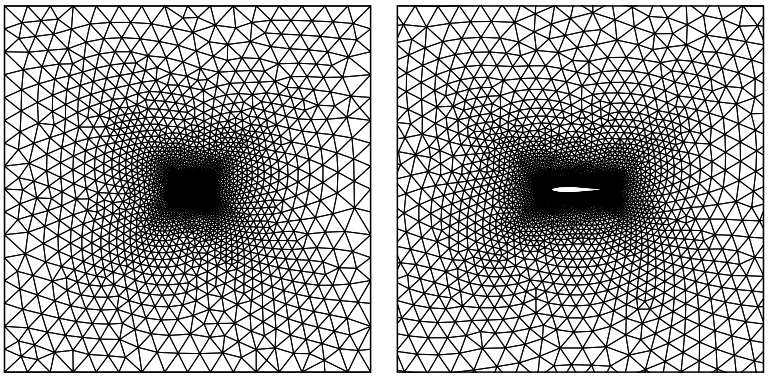

FIG. 3.15. *NACA*0012 *airfoil sample mesh. From left to right: the whole region, zoomed-in figure near airfoil.*

WENO scheme. Mach number and pressure distributions are shown in Figure 3.16. The reductions of density residual as a function of the number of iterations are shown in Figures 3.17 and 3.18, respectively. We can see that the fourth order WENO scheme has better resolution than the third order one and both of them could maintain a good convergence property for this problem.

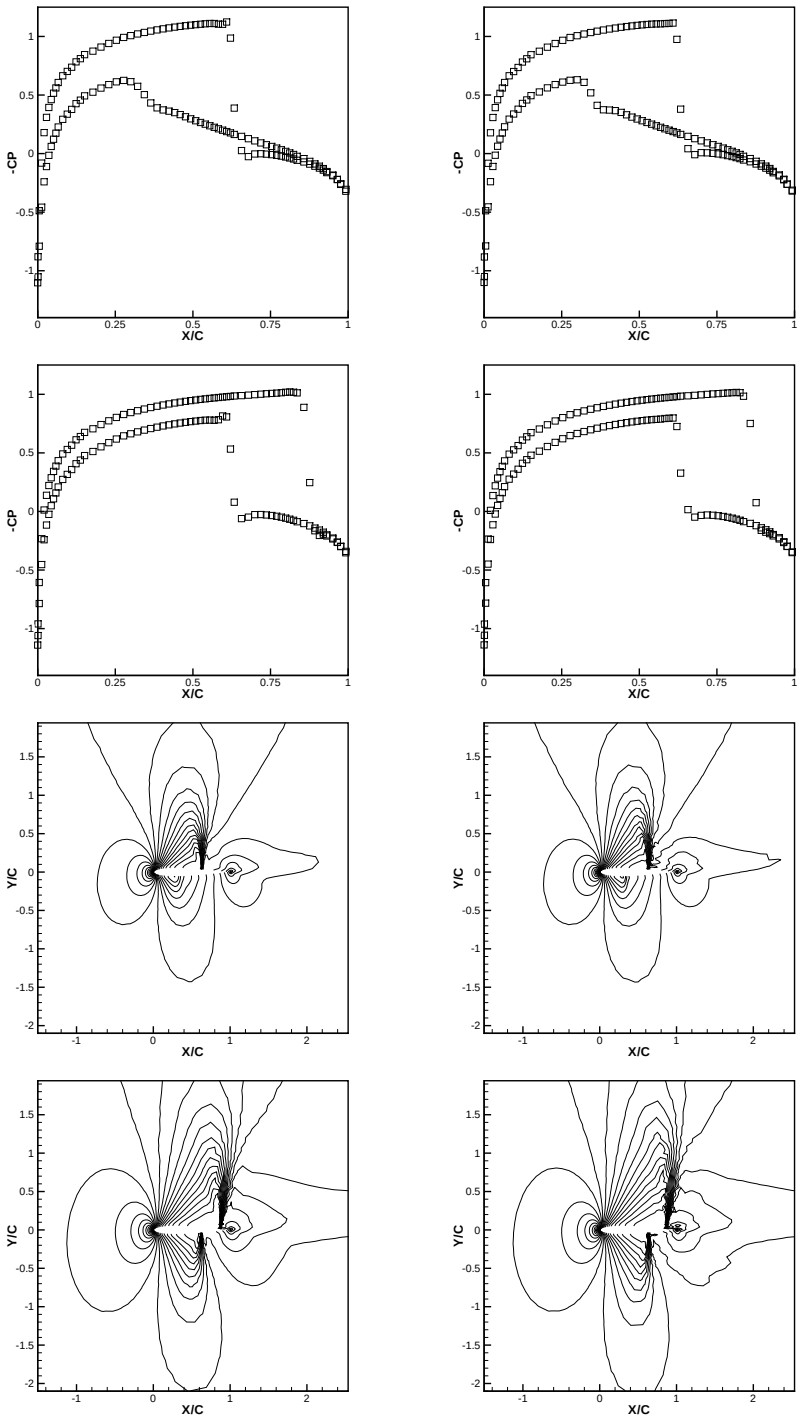

FIG. 3.16. *NACA*0012 *airfoil. From top to bottom:* $M_\infty = 0.8$, *angle of attack* $\alpha = 1.25°$, *pressure distribution;* $M_\infty = 0.85$, *angle of attack* $\alpha = 1°$, *pressure distribution;* $M_\infty = 0.8$, *angle of attack* $\alpha = 1.25°$, 30 *equally spaced mach number contours from* 0.172 *to* 1.325*;* $M_\infty = 0.85$, *angle of attack* $\alpha = 1°$, 30 *equally spaced mach number contours from* 0.158 *to* 1.357. *Left: the third order WENO* (1) *scheme; right: the fourth order WENO* (1) *scheme.*

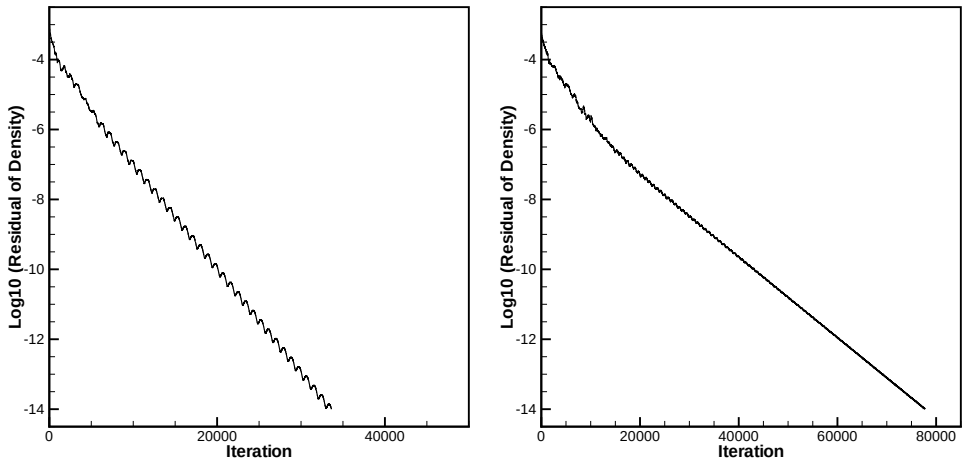

FIG. 3.17. *NACA*0012 *airfoil.* $M_\infty = 0.8$*, angle of attack* $\alpha = 1.25°$*. Reduction of density residual as a function of the number of iterations. Left: the third order WENO* (1) *scheme; right: the fourth order WENO* (1) *scheme.*

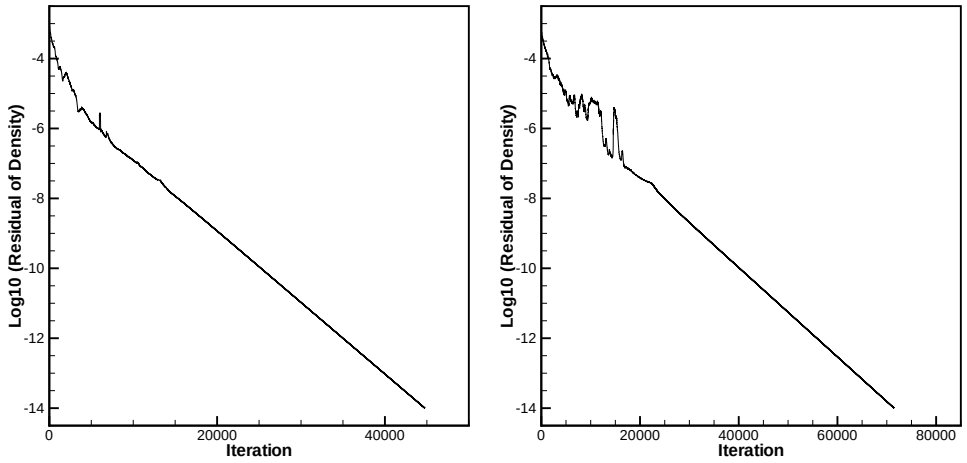

FIG. 3.18. *NACA*0012 *airfoil.* $M_\infty = 0.85$*, angle of attack* $\alpha = 1°$*. Reduction of density residual as a function of the number of iterations. Left: the third order WENO* (1) *scheme; right: the fourth order WENO* (1) *scheme.*

4. Concluding remarks. In this paper we investigate using a new type of third order and fourth order finite volume WENO schemes on triangular meshes. The main advantages of the new WENO schemes are their easy implementation on unstructured meshes, their compact property, the application of only 5 unequal sized spatial stencils for spatial reconstructions of different order WENO schemes in comparison with 10 stencils for the third order WENO scheme and 7 stencils for the fourth order WENO scheme [12], and that they could obtain high order accuracy in a smooth region simultaneously maintaining sharp shock transitions without redundantly considering the quality of the computational meshes. It is easy to get one big central stencil and four small biased/central stencils containing enough triangular cells. Then we

use the information defined on associated five unequal sized stencils to construct a quadratic/cubic polynomial and four linear polynomials in a least square sense and modify the quadratic/cubic polynomial by subtracting four linear polynomials with suitable positive constants for canceling the lower degree polynomials' contributions in the smooth region. By doing so, we could decrease the effectiveness of distorted geometries of the meshes and reduce the difficulty in calculating the linear systems for solving the optimal linear weights at different Gaussian quadrature points by means of designing a new linear weights choice principle. It is the first time that we can design any high order finite volume WENO schemes with the application of only five unequal sized spatial stencils on triangular meshes. Such a methodology is also applicable to constructing a third order finite volume WENO scheme with fewer spatial stencils on tetrahedral meshes [32]. Generally speaking, it is a promising method that could be extended to perform adaptive calculations, moving mesh simulations, arbitrary Lagrangian–Eulerian methods, and so on.

REFERENCES

[1] R. Abgrall, *On essentially non-oscillatory schemes on unstructured meshes: Analysis and implementation*, J. Comput. Phys., 114 (1993), pp. 45–58.

[2] R. Borges, M. Carmona, B. Costa, and W. S. Don, *An improved weighted essentially non-oscillatory scheme for hyperbolic conservation laws*, J. Comput. Phys., 227 (2008), pp. 3191–3211.

[3] J. Casper, *Finite-volume implementation of high-order essentially nonoscillatory schemes in two dimensions*, AIAA J., 30 (1992), pp. 2829–2835.

[4] J. Casper and H.-L. Atkins, *A finite-volume high-order ENO scheme for two-dimensional hyperbolic systems*, J. Comput. Phys., 106 (1993), pp. 62–76.

[5] M. Castro, B. Costa, and W. S. Don, *High order weighted essentially non-oscillatory WENO-Z schemes for hyperbolic conservation laws*, J. Comput. Phys., 230 (2011), pp. 1766–1792.

[6] M. Dumbser and M. Käser, *Arbitrary high order non-oscillatory finite volume schemes on unstructured meshes for linear hyperbolic systems*, J. Comput. Phys., 221 (2007), pp. 693–723.

[7] M. Dumbser, M. Käser, V. A. Titarev, and E. F. Toro, *Quadrature-free non-oscillatory finite volume schemes on unstructured meshes for nonlinear hyperbolic systems*, J. Comput. Phys., 226 (2007), pp. 204–243.

[8] O. Friedrichs, *Weighted essentially non-oscillatory schemes for the interpolation of mean values on unstructured grids*, J. Comput. Phys., 144 (1998), pp. 194–212.

[9] A. Harten, *Preliminary results on the extension of ENO schemes to two-dimensional problems*, in Proceedings, International Conference on Nonlinear Hyperbolic Problems, Saint-Etienne, 1986, C. Carasso et al., eds., Lecture Notes in Math. 1270, Springer-Verlag, Berlin, 1987, pp. 23–40.

[10] A. Harten and S. R. Chakravarthy, *Multi-Dimensional ENO Schemes for General Geometries*, ICASE Report, 1991, pp. 91–76.

[11] A. Harten, B. Engquist, S. Osher, and S. Chakravathy, *Uniformly high order accurate essentially non-oscillatory schemes*, III, J. Comput. Phys., 71 (1987), pp. 231–303.

[12] C. Hu and C.-W. Shu, *Weighted essentially non-oscillatory schemes on triangular meshes*, J. Comput. Phys., 150 (1999), pp. 97–127.

[13] G. Jiang and C.-W. Shu, *Efficient implementation of weighted ENO schemes*, J. Comput. Phys., 126 (1996), pp. 202–228.

[14] D. Levy, G. Puppo, and G. Russo, *Central WENO schemes for hyperbolic systems of conservation laws*, Math. Model. Numer. Anal., 33 (1999), pp. 547–571.

[15] D. Levy, G. Puppo, and G. Russo, *Compact central WENO schemes for multidimensional conservation laws*, SIAM J. Sci. Comput., 22 (2000), pp. 656–672.

[16] X. Liu, S. Osher, and T. Chan, *Weighted essentially non-oscillatory schemes*, J. Comput. Phys., 115 (1994), pp. 200–212.

[17] Y. Liu and Y. T. Zhang, *A robust reconstruction for unstructured WENO schemes*, J. Sci. Comput., 54 (2013), pp. 603–621.

[18] J. Qiu and C.-W. Shu, *On the construction, comparison, and local characteristic decomposition for high order central WENO schemes*, J. Comput. Phys., 183 (2002), pp. 187–209.

[19] J. Qiu and C.-W. Shu, *Hermite WENO schemes and their application as limiters for Runge-Kutta discontiuous Galerkin method* II: *Two dimensional case*, Comput. & Fluids, 34 (2005), pp. 642–663.
[20] J. Shi, C. Hu, and C.-W. Shu, *A technique of treating negative weights in WENO schemes*, J. Comput. Phys., 175 (2002), pp. 108–127.
[21] T. Sonar, *On the construction of essentially non-oscillatory finite volume approximations to hyperbolic conservation laws on general triangulations: Polynomial recovery, accuracy and stencil selection*, Comput. Methods Appl. Mech. Engrg., 140 (1997), pp. 157–181.
[22] C.-W. Shu, *Essentially non-oscillatory and weighted essentially non-oscillatory schemes for hyperbolic conservation laws*, in Advanced Numerical Approximation of Nonlinear Hyperbolic Equations, A. Quarteroni, ed., Lecture Notes in Math. 1697, Springer-Verlag, Berlin.
[23] C.-W. Shu and S. Osher, *Efficient implementation of essentially non-oscillatory shock-capturing schemes*, J. Comput. Phys., 77 (1988), pp. 439–471.
[24] C.-W. Shu and S. Osher, *Efficient implementation of essentially non-oscillatory shock capturing schemes* II, J. Comput. Phys., 83 (1989), pp. 32–78.
[25] V. A. Titarev, P. Tsoutsanis, and D. Drikakis, *WENO schemes for mixed-element unstructured meshes*, Commun. Comput. Phys., 8 (2010), pp. 585–609.
[26] P. Vankeirsbilck, *Algorithmic Developments for the Solution of Hyperbolic Conservation Laws on Adaptive Unstructured Grids*, Ph.D. thesis, Katholieke Universiteit Leuven, 1993.
[27] P. Woodward and P. Colella, *The numerical simulation of two-dimensional fluid flow with strong shocks*, J. Comput. Phys., 54 (1984), pp. 115–173.
[28] Y. T. Zhang and C.-W. Shu, *Third order WENO scheme on three dimensional tetrahedral meshes*, Commun. Comput. Phys., 5 (2009), pp. 836–848.
[29] X. Zhong and C.-W. Shu, *A simple weighted essentially nonoscillatory limiter for Runge-Kutta discontinuous Galerkin methods*, J. Comput. Phys., 232 (2013), pp. 397–415.
[30] J. Zhu and J. Qiu, *A new fifth order finite difference WENO scheme for solving hyperbolic conservation laws*, J. Comput. Phys., 318 (2016), pp. 110–121.
[31] J. Zhu and J. Qiu, *A new type of finite volume WENO schemes for hyperbolic conservation laws*, J. Sci. Comput., 73 (2017), pp. 1338–1359.
[32] J. Zhu and J. Qiu, *A new third order finite volume weighted essentially non-oscillatory scheme on tetrahedral meshes*, J. Comput. Phys., 349 (2017), pp. 220–232.
[33] J. Zhu, J. Qiu, C.-W. Shu, and M. Dumbser, *Runge-Kutta discontinuous Galerkin method using WENO limiters* II*: Unstructured Meshes*, J. Comput. Phys., 227 (2008), pp. 4330–4353.
[34] J. Zhu, X. Zhong, C.-W. Shu, and J. Qiu, *Runge-Kutta discontinuous Galerkin method using a new type of WENO limiters on unstructured meshes*, J. Comput. Phys., 248 (2013), pp. 200–220.